

Intrinsic Ferroelectric Switching in Two-Dimensional α - In_2Se_3

Liyi Bai,^{||} Changming Ke,^{||} Zhongshen Luo,^{||} Tianyuan Zhu, Lu You,* and Shi Liu*



Cite This: *ACS Nano* 2024, 18, 26103–26114



Read Online

ACCESS |



Metrics & More



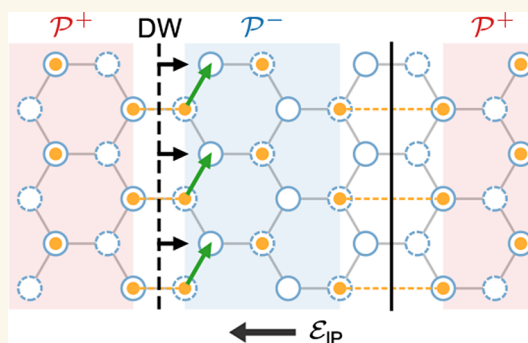
Article Recommendations



Supporting Information

ABSTRACT: Two-dimensional (2D) ferroelectric semiconductors present opportunities for integrating ferroelectrics into high-density ultrathin nanoelectronics. Among the few synthesized 2D ferroelectrics, α - In_2Se_3 , known for its electrically addressable vertical polarization, has attracted significant interest. However, the understanding of many fundamental characteristics of this material, such as the existence of spontaneous in-plane polarization and switching mechanisms, remains controversial, marked by conflicting experimental and theoretical results. Here, our combined experimental characterizations with piezoresponse force microscope and symmetry analysis conclusively dismiss previous claims of in-plane ferroelectricity in single-domain α - In_2Se_3 . The processes of vertical polarization switching in monolayer α - In_2Se_3 are explored with deep-learning-assisted large-scale molecular dynamics simulations, revealing atomistic mechanisms fundamentally different from those of bulk ferroelectrics. Despite lacking in-plane effective polarization, 1D domain walls can be moved by both out-of-plane and in-plane fields, exhibiting avalanche dynamics characterized by abrupt, intermittent moving patterns. The propagating velocity at various temperatures, field orientations, and strengths can be statistically described with a universal creep equation, featuring a dynamical exponent of 2 that is distinct from all known values for elastic interfaces moving in disordered media. This work rectifies a long-held misunderstanding regarding the in-plane ferroelectricity of α - In_2Se_3 , and the quantitative characterizations of domain wall velocity will hold broad implications for both the fundamental understanding and technological applications of 2D ferroelectrics.

KEYWORDS: 2D ferroelectrics, α - In_2Se_3 , domain wall dynamics, in-plane polarization, deep potential molecular dynamics



INTRODUCTION

For a ferroelectric thin film, the depolarization field that arises due to the imperfect screening of polarization bound charges on surfaces is inversely proportional to the thickness of the film.¹ The suppressed polarization along the direction of reduced dimensionality has been a main obstacle for the miniaturization of ferroelectric-based devices. Among the limited number of synthesized two-dimensional (2D) ferroelectrics, α - In_2Se_3 has garnered considerable attention, mainly because of its advantageous out-of-plane polarization (P_{OP}) in the monolayer limit.^{2–4} This characteristic allows for full utilization of the atomic thickness for the development of high-performance, ultrathin nanoelectronics.⁵ Notably, the 2D ferroelectricity in α - In_2Se_3 was first predicted theoretically based on density functional theory (DFT) calculations,² which was later confirmed experimentally.^{3,4} Several device prototypes, including ferroelectric channel transistor⁶ and synaptic ferroelectric semiconductor junction,⁷ have been fabricated using quasi-2D In_2Se_3 films with a thickness of tens of nanometers. In addition to forming the α phase, In_2Se_3 can

crystallize into the β' phase with in-plane polarization (P_{IP}) and the paraelectric β phase (Figure 1a).^{8–11} Leveraging both polymorphism and ferroelectricity of In_2Se_3 establishes a versatile platform for device design.¹²

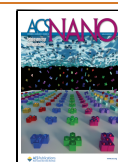
Recent experiments have demonstrated that van der Waals (vdW) stacked bilayers of nonferroelectric monolayers can be engineered into ferroelectrics through sliding and twisting,^{13–17} thus substantially expanding the family of 2D ferroelectrics possessing P_{OP} . Much like their bulk counterparts, the functional attributes of 2D ferroelectrics depend critically on the polarization response to external stimuli, whereas it is not clear whether various switching models developed for bulk ferroelectrics can be directly applied to

Received: May 19, 2024

Revised: August 31, 2024

Accepted: September 6, 2024

Published: September 16, 2024



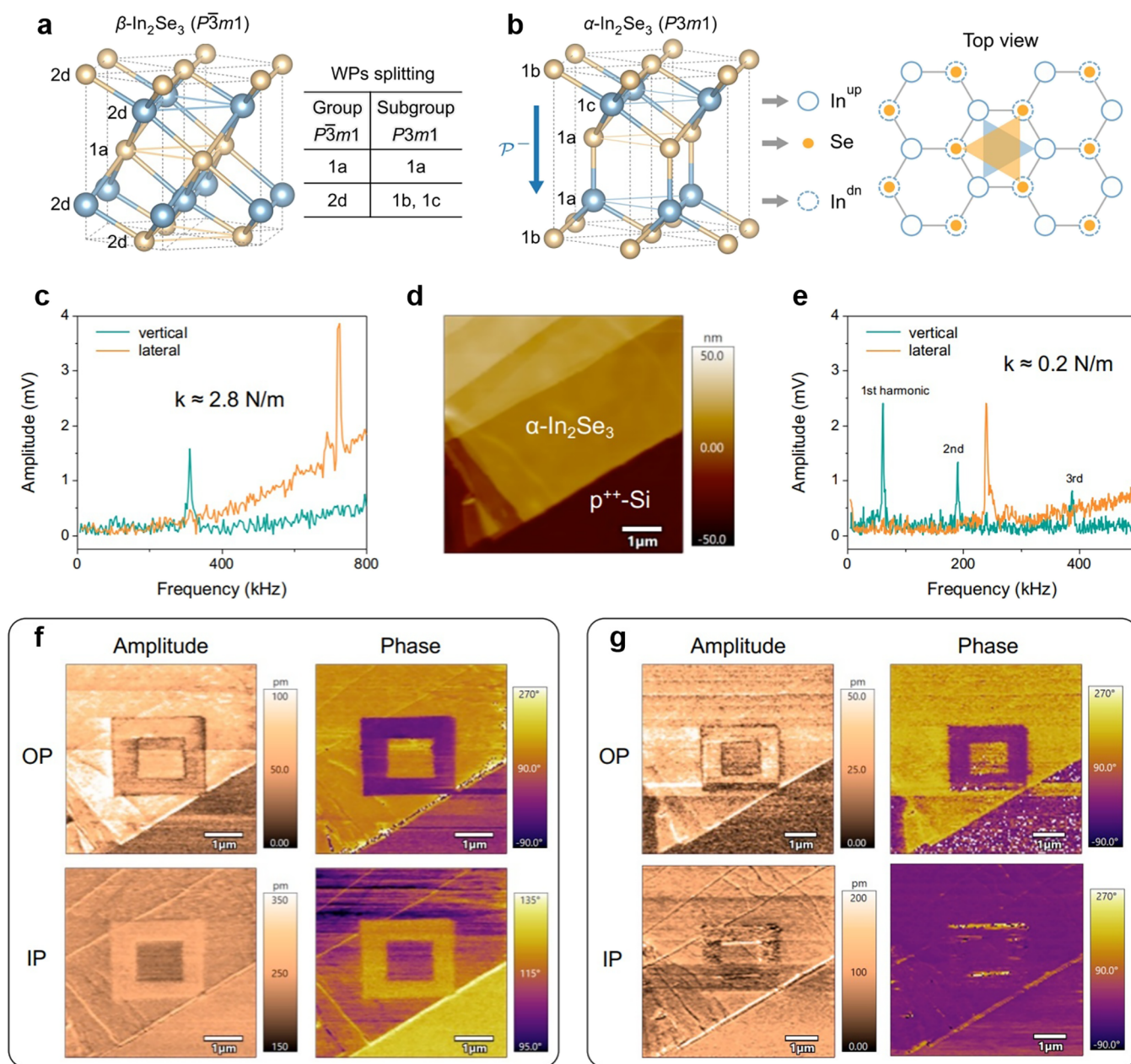


Figure 1. OP- and IP-PFM measurements on $\alpha\text{-In}_2\text{Se}_3$ using AFM probes with different force constants. Schematics of (a) paraelectric β phase and (b) ferroelectric α phase with Wyckoff positions (WPs) labeled. For simplicity, the top view of $\alpha\text{-In}_2\text{Se}_3$ does not display the outermost Se atoms. The table presents the splitting rules of WPs for the phase transition of $P\bar{3}m1 \rightarrow P3m1$. The In atoms in $\alpha\text{-In}_2\text{Se}_3$ occupy 1a and 1c orbit, respectively, which does not confirm to the $2d \rightarrow 1b/1c$ splitting rule for the symmetry break $P\bar{3}m1 \rightarrow P3m1$. (c) Vertical and lateral surface tuning spectra using a probe with (c) $k \approx 2.8$ N/m and (e) $k \approx 0.2$ N/m. (d) AFM topographic image of the measured $\alpha\text{-In}_2\text{Se}_3$ flake. (f) OP- and IP-PFM amplitude and phase images acquired by the probe with (f) $k \approx 2.8$ N/m and (g) $k \approx 0.2$ N/m.

reduced dimensions.¹⁸ At the most fundamental level, the controlled engineering of ferroelectric switching in 2D hinges on a quantitative characterization of the dynamics of 1D domain walls, which are nanoscale interfaces between differently polarized 2D domains. This endeavor has been particularly challenging due to the high temporal and spatial resolution required for both experimental and theoretical approaches, such that there is virtually no reported data on the velocity of 1D domain walls in 2D ferroelectrics. In this work, we use 2D $\alpha\text{-In}_2\text{Se}_3$ as a model system to investigate the switching mechanisms in 2D.

The structural origin of P_{OP} in monolayer $\alpha\text{-In}_2\text{Se}_3$ (space group $P3m1$) is unambiguous: it results from the shift of the

central Se layer along the z -axis that breaks the out-of-plane inversion symmetry (Figure 1b). Despite extensive studies, several specifics of ferroelectricity in 2D $\alpha\text{-In}_2\text{Se}_3$ remain unclear. Particularly, there is an ongoing debate regarding whether monolayer $\alpha\text{-In}_2\text{Se}_3$ exhibits electrically switchable in-plane effective polarization (P_{IP}). In the original paper predicting 2D ferroelectricity in monolayer $\alpha\text{-In}_2\text{Se}_3$,¹⁹ it was argued that it should also possess P_{IP} , mainly deduced from the cross-sectional crystal structure which suggests a lateral off-centered displacement of Se atom. However, as pointed out by follow-up studies,²⁰ the C_{3v} point group symmetry (out-of-plane 3-fold rotational axis) of $\alpha\text{-In}_2\text{Se}_3$ strictly prohibits in-plane switchable polarization (also referred to as *effective*

polarization in modern theory of polarization^{21,22}), according to Neumann's principle. This is evident from the top view of α -In₂Se₃, similar to *h*-BN (Figure S1), which is invariant with respect to a 3-fold rotation thus nullifying any in-plane spontaneous polarization. Nevertheless, multiple experimental studies have reported switching-like behaviors when in-plane electric fields (ϵ_{IP}) are applied to α -In₂Se₃ thin films.^{23,24}

Another experiment-theory conundrum for 2D α -In₂Se₃ involves the coercive field that switches P_{OP} . Previous DFT investigations have indicated a rather low switching barrier of ≈ 66 meV per unit cell (uc) in monolayer α -In₂Se₃,¹⁹ yet the observed out-of-plane switching field is commonly above 1 V/nm (10 MV/cm),⁴ several orders of magnitude higher than that for PbTiO₃-based perovskite ferroelectrics (≈ 10 kV/cm)²⁵ which actually have larger switching barriers (≈ 200 meV/uc). The low barrier predicted by DFT does not support "dipole locking mechanism", which proposes that the locked out-of-plane and in-plane motion of the middle Se atom would lead to a large barrier.⁴ We note that this terminology has its own issues, as it could be mistakenly interpreted as the locking between out-of-plane and in-plane net dipoles, despite the original work explicitly stating that there is only in-plane asymmetry (see additional discussions in Supplementary Section I). This asymmetry does not lead to in-plane net electric dipole (due to 3-fold rotational symmetry), but it allows for effective in-plane second-order optical dipole emission. Such experiment-theory conundrum appears to be a common feature for vdW bilayers exhibiting sliding ferroelectricity. For example, the DFT-predicted switching barrier for Bernal-stacked *h*-BN possessing sliding ferroelectricity is only 8 meV/uc,²⁶ yet the experimental switching field is on the order of 0.1 V/nm.^{13,27}

To summarize, currently there is no consensus, be it experimental or theoretical, on several key questions: (i) Does monolayer α -In₂Se₃ exhibit switchable P_{IP} ? (ii) Why does 2D α -In₂Se₃, similar to vdW bilayers of stacking-engineered ferroelectricity, exhibit such a high out-of-plane switching field? (iii) What are the polarization switching dynamics involved in 2D domains and 1D walls? Here, we address these questions with both experimental characterizations and a multiscale modeling approach that combines symmetry analysis, DFT calculations, and deep-learning-assisted large-scale molecular dynamics (MD) simulations.

RESULTS AND DISCUSSION

Symmetry Analysis of α -In₂Se₃. Monolayer α -In₂Se₃ is in the space group of $P3m1$, while the bulk forms adopting 3R and 2H stacking orders are in the space groups of $P6_3mc$ and $R3m$, respectively. All these space groups exhibit a 3-fold rotational axis along z (the out-of-plane direction for the monolayer). Proper symmetry analysis should lead to a straightforward conclusion: there is only in-plane piezoelectricity due to the in-plane inversion symmetry breaking, but there is no in-plane ferroelectricity. The in-plane asymmetry of α -In₂Se₃ is similar to that in 2H or 3R MoS₂ and *h*-BN. It is possible that residual uniaxial strains in α -In₂Se₃ samples could disrupt the 3-fold rotational symmetry, and the piezoelectric effect gives rise to finite but nonreversible P_{IP} .

The resilience of P_{OP} against the depolarization field in 2D α -In₂Se₃ can also be understood with a symmetry argument, viewing the switching process from the ferroelectric to the reference paraelectric phase as an electric field-driven phase transition. The Landau theory of group-subgroup structural

phase transitions presumes that transitions result from the condensation of either a single or a group of collective degrees of freedom, conforming to a single irreducible representation (irrep) of the space group for the high-symmetry phase. Within a space group, atoms occupy specific positions known as Wyckoff positions (or orbits), defined by their symmetry properties within the space group. Wyckoff orbit splitting refers to the phenomenon where a set of equivalent atomic positions in a crystal becomes distinct and nonequivalent due to a reduction in symmetry during a group-subgroup phase transition. Each type of group-subgroup transition has its own set of restrictions on how these splittings can occur (see the example of the paraelectric-ferroelectric phase transition of PbTiO₃ in Figure S2). We find that though paraelectric β -In₂Se₃ (space group $P\bar{3}m1$) and ferroelectric α -In₂Se₃ (space group $P3m1$) conform to the group-subgroup relationship, the $\beta \leftrightarrow \alpha$ transition cannot be realized by a structural distortion associated with an irrep of $P\bar{3}m1$, because the atomic occupations in β -In₂Se₃ and α -In₂Se₃ do not conform to the required splitting of Wyckoff positions. Specifically, the In atoms occupy the 2d Wyckoff orbits in β -In₂Se₃, while the two In atoms in α -In₂Se₃ occupy 1a and 1c orbit, respectively, violating the allowed splitting rule of $2d \rightarrow 1b/1c$ associated with $P\bar{3}m1 \rightarrow P3m1$ (see Figure 1a,b). This is fundamentally different from (proper) perovskite ferroelectrics, where a polar soft mode identified by an irrep serves as the primary order parameter responsible for the paraelectric-ferroelectric phase transition.²⁸ Given that a depolarization field mainly suppresses the displacive distortion associated with the polar soft mode, we propose that P_{OP} in 2D α -In₂Se₃ is protected by a principle we call "splitting restriction", which refers to the forbidden splitting of Wyckoff orbits during the postulated phase transition. We highlight that the same mechanism also plays a role in the stabilization of P_{OP} emerged in sliding and moiré ferroelectricity^{29–32} (see detailed discussions about Bernal-stacked *h*-BN in Supplementary Section VII). Additionally, the splitting restriction principle predicts that $\beta \rightarrow \beta'$ could be favored over $\beta \rightarrow \alpha$, which is consistent with our Raman spectroscopy characterizations of 2H- α -In₂Se₃ during a heating-cooling cycle (see Supplementary Section II).

Piezoelectric Response Microscopy Characterizations of α -In₂Se₃. The aforementioned symmetry analysis resoundingly indicates the absence of switchable P_{IP} in α -In₂Se₃, contrasting to a flurry of research studies that have claimed its existence. Nearly all reports of the presence of P_{IP} in 2D α -In₂Se₃ depended on measurements of piezoresponse force microscopy (PFM) with the Dual AC Resonance Tracking (DART) mode.^{3,23,24,33–35} We will first argue, based on fundamental PFM theory, that acquiring in-plane PFM (IP-PFM) signal in α -In₂Se₃ is not possible. In IP-PFM studies, the piezoresponse signal is related to the torsional motion of the atomic force microscopy (AFM) probe, which is caused by the shear strain of the sample under vertical electric field. The relevant piezoelectric coefficient in this process is d_{35} (or d_{34}), where the subscript 5 (or 4) denotes the induced shear strain in xz (or yz) plane under Voigt notation (Figure S4). However, for monolayer α -In₂Se₃ with a space group $P3m1$, both d_{35} and d_{34} components are zero within its piezoelectric tensorial matrix. The same situation applies to bulk α -In₂Se₃ with 2H or 3R stacking order (Figure S5). It is worth noting that the symmetric distribution of the IP electric field component of the AFM probe in conjunction with the 3-fold

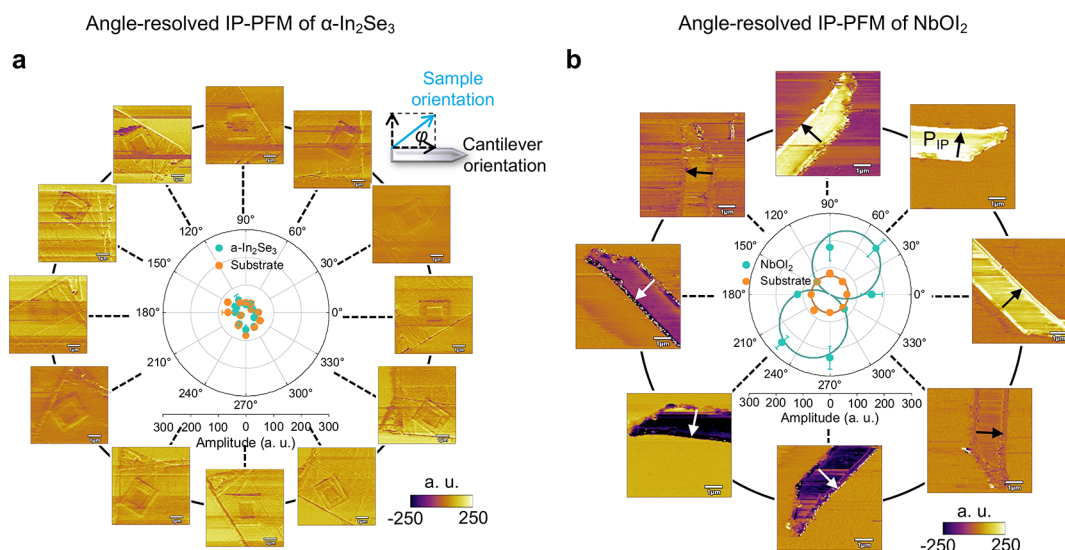


Figure 2. Comparative study by angle-resolved IP-PFM. Angle-resolved IP-PFM images of (a) α - In_2Se_3 and (b) NbOI_2 . The polar plots in the center of (a) and (b) are the extracted mean amplitude of each PFM image at respective azimuthal angle. The measurement conditions were fixed for two samples.

rotational symmetry also prohibits the detection of nonzero IP piezoelectric tensor elements (e.g., d_{22}).

Second, it is well-known in the PFM community that out-of-plane and in-plane deformation signals are strongly convoluted in practical measurements.^{36,37} Thus, special care and a proper measurement protocol are required to unambiguously separate the vertical and lateral contributions with correct interpretations of the results, which were seriously lacking in previous studies of α - In_2Se_3 (see case-by-case analysis of the previous reports in [Supplementary Section III](#)). Herein, we perform a comparative PFM study on α - In_2Se_3 thin flakes exfoliated onto highly doped silicon substrate ([Figure 1d](#)) by using two AFM probes with different force constants. One probe has a force constant (k) of ≈ 2.8 N/m, similar to those widely used in previous reports, while the other is much softer ($k \approx 0.2$ N/m) with better torsional sensitivity.³⁸ Both the out-of-plane and in-plane surface tuning spectra for both probes were recorded first to determine the contact resonance between the probe and the sample for the subsequent DART PFM measurements. As shown in [Figure 1c,e](#), the resonant peaks for vertical deflection and lateral torsion modes are distinct from each other for both probes. The α - In_2Se_3 sample used here contains mixed 2H and 3R stacking, as confirmed by our Raman and SHG measurements ([Figure S7](#)). Similar incommensurate stacking structure is commonly observed in chemical vapor-grown In_2Se_3 single crystals.^{39,40} Such sample, however, helps us exclude the existence of P_{IP} in both stacking types as detailed below.

Next, OP- and IP-PFM images are acquired using both probes driven by an AC voltage at their respective first harmonic frequencies. A box-in-box pattern was written by a DC biased probe in advance, as a reference for the following measurements. For OP-PFM, both probes provide strong piezoresponse amplitude on the α - In_2Se_3 surface compared with the Si substrate. Additionally, the phase images show sharp 180° difference between upward and downward domains, confirming the noticeable piezoresponse (d_{33}) in the out-of-plane direction. For IP-PFM, however, although we observe sizable “amplitude signal”, it is not distinguishable between α - In_2Se_3 and the nonpiezoelectric Si substrate. As mentioned, this spurious signal originates from the electronic

background of the lock-in amplifier at high frequency. The phase image obtained by the stiff probe exhibits a domain pattern identical to the OP-PFM image ([Figure 1f](#)), yet the phase difference between oppositely polarized domains is much less than 180° . Thus, the observed IP piezoresponse signal is probably a crosstalk effect from the OP signal.^{36,37} By using a soft probe, this effect is reduced, but still visible ([Figure 1g](#)).

Another important practice in PFM to confirm the intrinsic in-plane response is to perform an angular-resolved lateral PFM by rotating the sample at different azimuthal angles with regard to the AFM cantilever.^{38,41} We carry out a comparative study by conducting angle-resolved IP-PFM on both 2H α - In_2Se_3 and NbOI_2 with known in-plane ferroelectricity under the same measurement condition, with the results summarized in [Figure 2](#). The measured IP-PFM amplitude is maximized when the direction of P_{IP} is perpendicular to the cantilever axis and minimized when they are parallel to each other. Hence, we should expect the IP-PFM amplitude to follow an absolute sinusoidal function with a period of 180° . This is exactly what is observed in the central polar plot of [Figure 2b](#) for NbOI_2 , and the in-phase signal also changes its sign (phase reversal) when the sample is rotated by 180° . In stark contrast, the α - In_2Se_3 sample with a prewritten box-in-box pattern shows no periodic modulation in both IP-PFM amplitude and phase ([Figure 2a](#)), suggesting the measured lateral response does not originate from intrinsic in-plane piezoresponse. Given the above symmetry analysis and experimental results, we can safely exclude the existence of P_{IP} in both 2H and 3R α - In_2Se_3 .

The out-of-plane piezoresponse and polarization, on the contrary, is confirmed ([Figure 1](#)) in our PFM investigations. We note that the out-of-plane switching field is extremely large, consistent with the prediction of splitting restriction principle. In an upward domain of a 30 nm-thick flake on highly doped Si, it is only possible to obtain a minor hysteresis loop (incomplete switching) under a DC voltage up to 9 V ([Figure S8d](#)), while no sign of switching is observed in the downward domain ([Figure S8e](#)). At such a high field, irreversible surface modification due to the electrochemical process starts to take place ([Figure S8a](#)). The results indicate that the out-of-plane

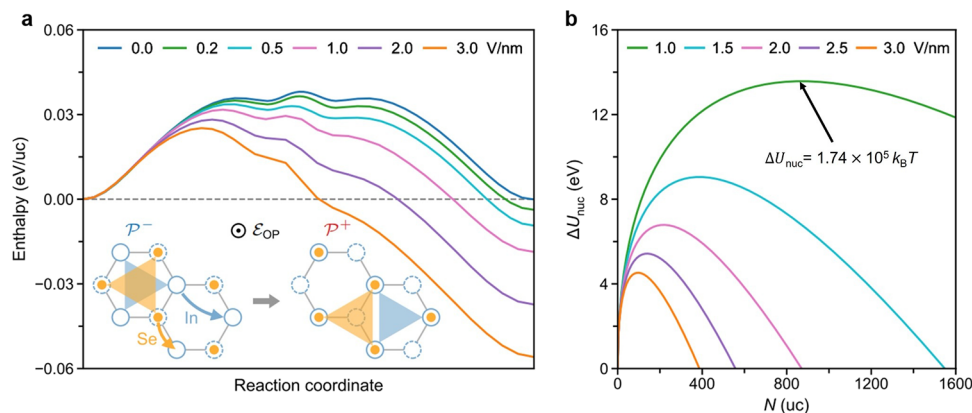


Figure 3. Domain switching in monolayer α - In_2Se_3 . (a) Minimum energy paths of polarization reversal identified with DFT-based NEB for various ϵ_{OP} magnitudes. The inset illustrates primary atomic movement patterns during this low-barrier switching pathway: entire layers of In and Se atoms need to move laterally in the same direction. This pathway is the same as the one reported in ref 19. (b) Analytical nucleation energy (ΔU_{nuc}) computed with DFT and MD parameters as a function of nucleus size (N) across various strengths of ϵ_{OP} .

coercive field is possibly beyond 3 MV/cm. For comparison, vdW ferroelectric CuInP_2S_6 with a similar thickness shows a coercive field below 1 MV/cm under the same measurement condition (Figure S8f). Interestingly, we find that the switching field is greatly reduced when the biased AFM probe is scanning on the sample surface, which could explain the widely reported domain switching behaviors in the literature. As detailed by our theoretical calculations below, it is indeed much easier to drive polarization switching through domain wall motions with an in-plane electric field despite the lack of in-plane ferroelectricity in monolayer α - In_2Se_3 .

Domain Switching in 2D α - In_2Se_3 . We now address the second experiment-theory conundrum: why experimentally a large out-of-plane electric field (ϵ_{OP}) is required to switch α - In_2Se_3 , despite the identification of a low-barrier pathway using the DFT-based nudged elastic band (NEB) technique. By carefully designing a pathway that connects the upward polarized and downward polarized monolayer α - In_2Se_3 , Ding *et al* obtained a NEB barrier (ΔU^{NEB}) of 66 meV/uc.¹⁹ Our calculated value for the same pathway is 40 meV/uc (Figure 3a), due to the usage of more intermediate images and tighter convergence threshold. However, a critical issue with NEB is that this method requires the manual construction of an initial pathway, which can potentially be subject to human bias, and there is no guarantee that such a manually designed pathway can be physically activated by ϵ_{OP} . Indeed, we find that this low-barrier pathway involves concerted lateral shifts of entire layers of In and Se atoms (see inset of Figure 3a), coupled with out-of-plane displacements that reverse P_{OP} . We suggest that it is highly improbable for ϵ_{OP} to activate this process: In and Se atoms, bearing opposite charges, should move in opposite directions under the influence of ϵ_{OP} , rather than moving in the same direction as assumed in NEB calculations. We further perform finite-field NEB calculations with varying ϵ_{OP} magnitudes and confirm that ΔU^{NEB} is weakly dependent on field strength: even an intense ϵ_{OP} of 3.0 V/nm (30 MV/cm) only moderately reduces the barrier (Figure 3a). This corroborates with the splitting restriction principle that suggests the absence of a symmetry-adapted polar mode for efficient $P_{\text{OP}}-\epsilon_{\text{OP}}$ coupling.

Another aspect is that ΔU^{NEB} corresponds to the barrier for a homogeneous switching mechanism during which all dipoles respond synchronously to ϵ_{OP} without nucleating oppositely

polarized domains. This overlooks the energy costs involved in creating interfaces that separate the newly formed nucleus and the surrounding domain. The difficulty of reversing P_{OP} in an ideal 2D domain of α - In_2Se_3 via ϵ_{OP} is further corroborated by our large-scale MD simulations that employs a deep neural network-based force field trained with a large database of ab initio energies and atomic forces from $\approx 25,000$ configurations of In_2Se_3 ⁴² (see Methods). We observe that a single-domain monolayer, constructed using an 18,000-atom supercell, is immune to ϵ_{OP} at 300 K (no switching detected within a simulation period of 3 ns), even when exposed to giant field strengths achievable in experimental setups. Only at an elevated temperature of 373 K is a nucleus formed with P_{OP} aligned with ϵ_{OP} of 3.0 V/nm (Figure S13). The change in the energy associated with the formation of a 2D nucleus containing N unit cells can be approximated as⁴³

$$\Delta U_{\text{nuc}} = -2N\epsilon_{\text{OP}}p_u + g\sqrt{N}\sigma_i \quad (1)$$

where p_u is the out-of-plane electric dipole moment per unit cell, σ_i is the (averaged) interface energy per unit-cell length of the boundary that separates the nucleus and the parent domain, and g is a geometric factor depending on the nucleus shape. Detailed derivations for eq 1 are provided in Supplementary Section VIII. Using $p_u = 0.09 \text{ e}\text{\AA}$ computed with DFT, $\sigma_i = 0.23 \text{ eV}$ and $g = 8/\sqrt{3}$ both extracted from MD, Figure 3b displays ΔU_{nuc} as a function of N for various field strengths, and the maximum of the plot determines the nucleation barrier (ΔU_{nuc}^*) and the size of the critical nucleus (N^*). For example, at $\epsilon_{\text{OP}} = 1.0 \text{ V/nm}$, the nucleation barrier is $\approx 1.74 \times 10^5 k_B T$, indicating an extremely low nucleation probability at room temperatures even under a high electric field. The high 1D interfacial energy σ_i and the small magnitude of p_u together make it energetically challenging to switch a 2D domain in monolayer α - In_2Se_3 . Under experimental conditions, the presence of defects could reduce the nucleation barrier by reducing σ_i .

Domain-Wall-Assisted Ferroelectric Switching. We will now demonstrate that pre-existing 1D domain walls can lower the switching field dramatically. When viewed from the out-of-plane direction of a single domain, the two layers of In atoms resemble the hexagonal lattice of monolayer h -BN with a (projected) bond length of a , while middle-layer Se atoms occupy only one type of lattice site (Figure 1b). There exist

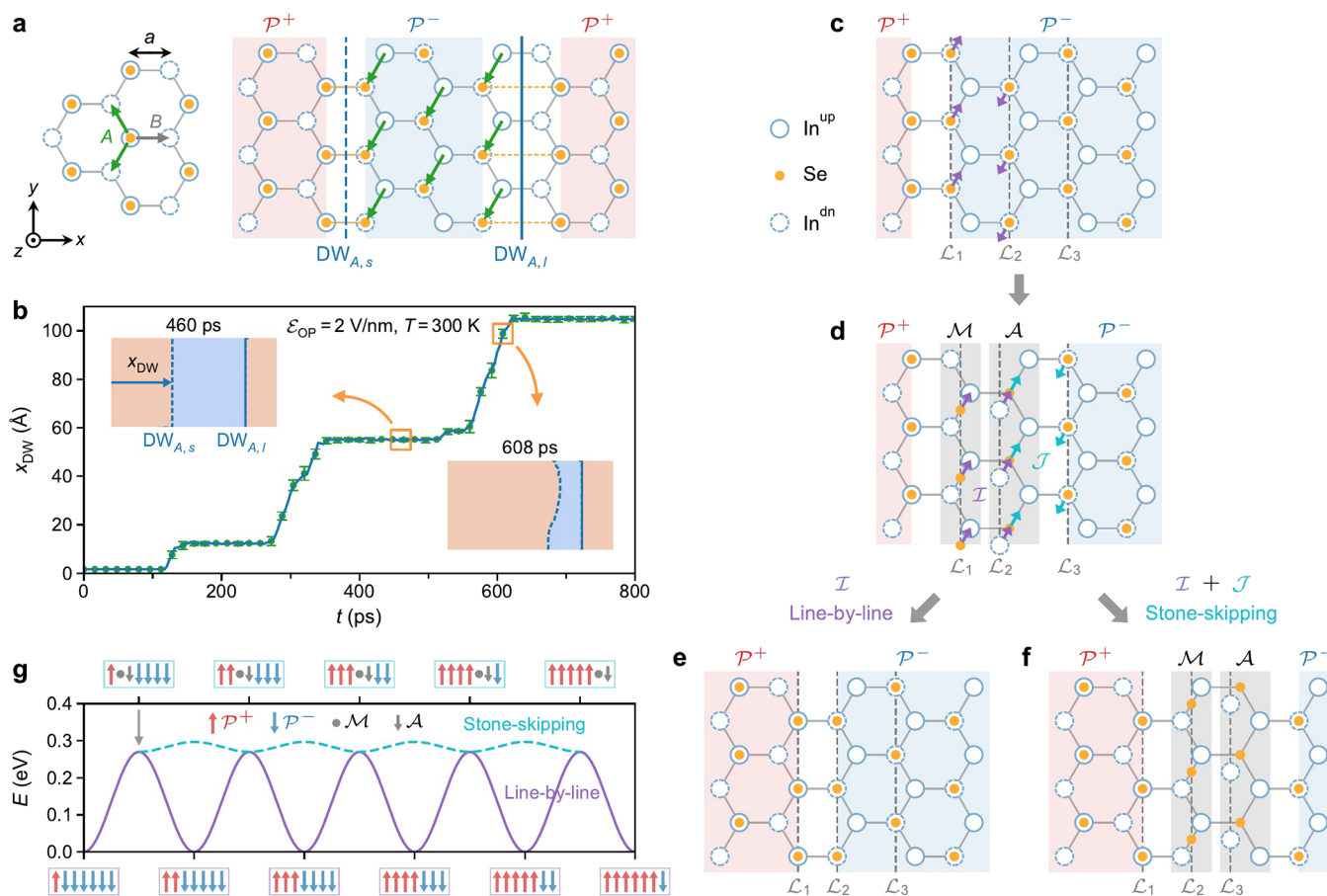


Figure 4. Avalanche dynamics of 1D domain walls driven by ϵ_{OP} in 2D α - In_2Se_3 . (a) Formation of 1D domain walls. The 180° walls separating P^+ and P^- domains can be created by an in-plane shift of a section of middle-layer Se atoms in either direction A or B by a distance of a , accompanied by an out-of-plane shift that flips the polarization. Type-A walls can be categorized as $DW_{A,s}$ characterized by short Se–Se bonds at the wall and $DW_{A,l}$ featuring large Se–Se separations. The green arrows denote the shift directions of Se atoms from their initial positions to the final positions. (b) Temporal evolution of the averaged position (x_{DW}) of $DW_{A,s}$ driven by ϵ_{OP} obtained from MD simulations of a 4000-atom supercell. $DW_{A,l}$ is immobile while $DW_{A,s}$ moves abruptly and intermittently, indicating avalanche dynamics. The error bar scales with the geometrical roughness (global width) of the wall. The insets illustrate the flatness of $DW_{A,s}$ at 460 and 608 ps (dynamic roughening). (c–f) depict two mechanisms of $DW_{A,s}$ motion derived from MD. Driven by ϵ_{OP} , $DW_{A,s}$ in (c) evolves to a transient interface MA in (d) via $P^-@L_1 \rightarrow M@L_1$ and $P^-@L_2 \rightarrow A@L_2$. Immediately following that, two atomic movement patterns denoted as I and J in (d) are possible. The concerted occurrence of I and J results in fast sideways movement of MA in (f). The failure of movement J recovers the Miller-Weinreich line-by-line mechanism in (e). (g) Schematics of energy profiles for line-by-line mechanism (solid line) and stone-skipping-like mechanism (dashed line). The bursts of domain wall motions in (b) are attributed to the fast-moving MA interface and the periods of inactivity are due to the reactivation of $DW_{A,s}$.

four variants of 180° domain walls, grouped into two pairs (A and B), that can be generated by an in-plane shift of a section of middle-layer Se atoms along the direction connecting In atoms by a distance of a accompanied by an out-of-plane shift that flips the polarization direction. As illustrated in Figure 4a, for each pair, there is a wide domain wall characterized by long Se–Se separations (e.g., $DW_{A,l}$) and a narrow domain wall featuring short Se–Se bonds (e.g., $DW_{A,s}$). We focus on type-A walls for their greater thermodynamic stability compared to type-B walls (see Supplementary Section IX). Our MD simulations further show that only $DW_{A,s}$ is movable by ϵ_{OP} ; $DW_{A,l}$ is immobile, consistent with its large barrier of 0.7 eV for domain wall motion, as predicted by DFT-based NEB calculations (see Table S2 in Supporting Information). The temporal evolution of the averaged position of $DW_{A,s}$ driven by ϵ_{OP} (Figure 4b) unveils two characteristics that differ distinctly from 2D domain walls in bulk ferroelectrics.^{43,44} First, the motion of $DW_{A,s}$ exhibits avalanche dynamics,⁴⁵ wherein this 1D interface moves abruptly and intermittently. The

distributions of the lifetimes of avalanche processes can be found in Supplementary Section X. Second, $DW_{A,s}$ acquires dynamic roughening: the initially flat wall becomes curved during its motion. The geometrical roughness, represented as error bars in Figure 4b, is characterized by a global width of ≈ 1.8 Å.

By analyzing MD trajectories with a fine time resolution down to femtoseconds, we identify a “stone skipping”-like mechanism that explains the two intrinsic features of $DW_{A,s}$ motion emerged in the absence of defects (disorder pinning). As depicted in Figure 4c, in the presence of ϵ_{OP} , a line of Se atoms (L_1) closest to the boundary move toward the bottom of nearby In^{up} atoms (denoted as $P^-@L_1 \rightarrow M@L_1$). Simultaneously, a line of In^{dn} atoms (L_2) shift toward those Se atoms of L_1 (denoted as $P^-@L_2 \rightarrow A@L_2$). This contrasts with the layer-by-layer switching mechanism pioneered by Miller and Weinreich for sideways motion of 2D domain walls.⁴⁶ Here, the movement of 1D $DW_{A,s}$ engages two lines of atoms and is

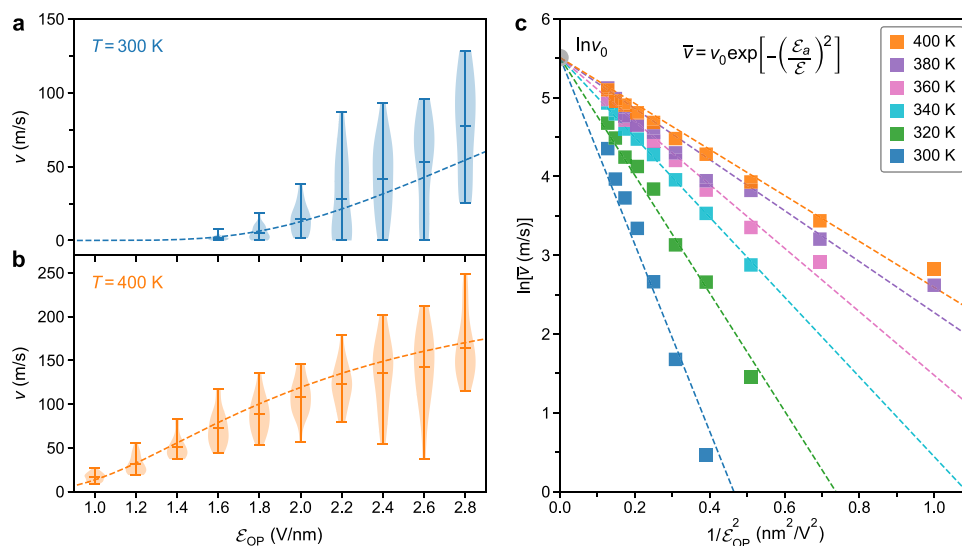


Figure 5. Velocity of 1D domain walls driven by ϵ_{OP} in 2D α - In_2Se_3 . Violin plot of domain wall velocity (v) at (a) 300 K and (b) 400 K. The mean velocity \bar{v} is fitted to eq 2 that describes a creep process. We find $v_0 = 247$ m/s and $\mu = 2$. (c) Plot of $\ln(\bar{v})$ versus $1/\epsilon_{OP}^2$ curves for different temperatures. All linear fits (dashed lines) converge at the same intercept corresponding to $v_0 = 247$ m/s.

somewhat reminiscent of the hypothesized “nuclei stacking” that is assumed to occur in a high-field-induced mobile rough wall (though rarely observed).⁴⁷ The transient interface, $M@L_1$ and $A@L_2$, can jointly serve as a moving front (Figure 4d). Specifically, subsequent processes of $A@L_2 \rightarrow M@L_2$ and $P^-@L_3 \rightarrow A@L_3$, achieved via atomic movement pattern J (Figure 4d), effectively move the MA interface sideways by a distance of a (Figure 4f). At steps where movement J does not take place, the line-by-line switching mechanism is recovered as the net outcome is $P^-@L_1 \rightarrow P^+@L_1$ (Figure 4e). We propose that the MA interface is an “emergent” high-energy interface that only needs to overcome a small kinetic barrier to move (see the dashed line in Figure 4g), analogous to a swiftly skipping stone on water. The probabilistic failure of movement J could trigger the relaxation of MA to a flat, low-energy interface ($DW_{A,s}$), the movement of which must overcome a large barrier (see the solid line in Figure 4g). This stone-skipping-like mechanism intuitively explains the bursts of domain wall motions (attributable to the emergent fast-moving MA interface) separated by periods of inactivity (due to the reactivation of $DW_{A,s}$). The dynamic roughening of $DW_{A,s}$ manifested as a wavy moving front (see MD snapshots in Figure S18), is a consequence of the interplay between two distinct mechanisms of domain wall motion along an extended 1D interface. Across larger length scales, specific sections of the interface progress through the slower, line-by-line mechanism, while other segments advance more rapidly via the stone-skipping-like mechanism. This differential speed of movement along the interface’s length results in the curvature during its motion. We note that during the period when the average position of the wall remains unchanged, the wall still exhibits significant dynamics: the interface fluctuates around the average position (see Figure S19). This behavior is indicative of a thermally driven activation process.

We use MD simulations to quantitatively estimate the velocity (v) of $DW_{A,s}$ over a wide range of temperatures (T) and ϵ_{OP} . It is noted that the value of v is calculated by measuring the distance that the wall traverses within a specific time frame, while also taking into account the periods of

inactivity when the wall is stationary. Due to the inherent avalanche dynamics, the values of v , obtained from multiple MD trajectories, exhibit a considerable fluctuation for a specific ϵ_{OP} and T , as shown by the violin plots at 300 and 400 K (Figure 5a,b). Even in the absence of defects, we discover that the mean 1D domain wall velocity, \bar{v} , can be well described with a creep process as^{48,49}

$$\bar{v} = v_0 \exp\left[-\left(\frac{\epsilon_a}{\epsilon}\right)^\mu\right] \quad (2)$$

where v_0 is the domain wall velocity under an infinite field, ϵ_a is the temperature-dependent activation field. Within a statistical description of domain wall motion as a critical phenomenon, that is, an elastic interface moving in random media, μ is the creep exponent that depends on the dimensionality of the interface and the universality class of the disorder landscape pinning the interface.²⁹ As depicted in Figure 5c, the plots of $\ln(v)$ versus $1/\epsilon_{OP}^2$ curves yield linear relationships across a broad spectrum of field strengths (1.0–2.8 V/nm) and various temperatures (300–400 K). Notably, all linear fits converge at the same intercept that corresponds to $v_0 = 247$ m/s. This serves as a strong evidence for a creep exponent, $\mu = 2$, higher than the well-known value of $\mu = 0.25$ for 1D magnetic domain walls in ultrathin magnetic films²⁹ as well as $\mu = 1$ for 2D ferroelectric domain walls in typical perovskite ferroelectrics.^{43,50} We propose ϵ_{OP} -driven creep motion of $DW_{A,s}$ in monolayer α - In_2Se_3 probably belongs to an entirely unreported universality class. A higher value of creep exponent implies that this interface is more sensitive to changes in the magnitude of ϵ_{OP} , especially at low driving forces, which is advantageous for fine-tuning domain wall mobility. Moreover, we observe the absence of an intrinsic creep–depinning transition, even at a colossal field strength of 2.8 V/nm (28 MV/cm), likely attributable to the small Born effect charges (0.49 for In and -0.45 for Se) in the out-of-plane direction: the weak ϵ_{OP} – P_{OP} coupling is insufficient to reduce the barrier of domain wall motion compared to thermal fluctuations, thus leading to persistent creep behavior of $DW_{A,s}$.

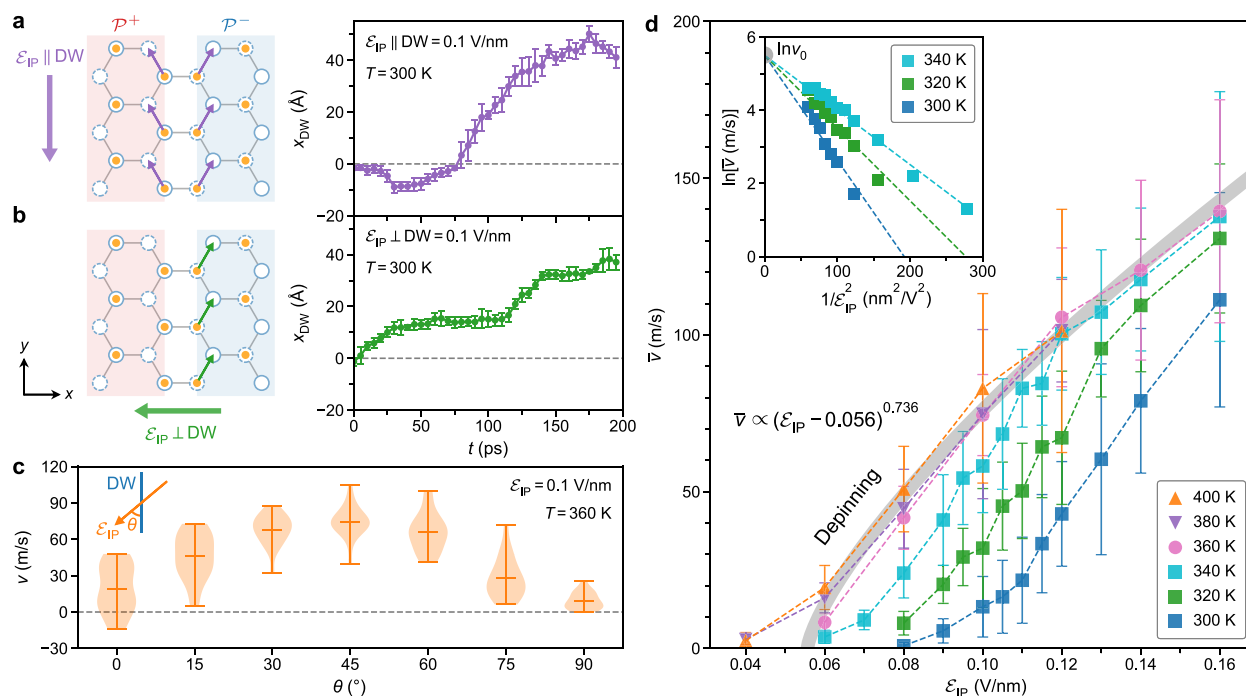


Figure 6. Dynamics of 1D domain walls driven by ϵ_{IP} in 2D α - In_2Se_3 . Temporal progression of $\text{DW}_{A,s}$ in the presence of ϵ_{IP} applied (a) parallel to the wall ($\epsilon_{IP} \parallel \text{DW}$) and (b) perpendicular to the wall ($\epsilon_{IP} \perp \text{DW}$), revealing avalanche dynamics in both cases. The field strength is 0.1 V/nm. (c) Violin plot of domain wall velocity as a function of the relative orientation (θ) between ϵ_{IP} and the wall at 360 K. (d) T - and ϵ_{IP} -dependent mean velocity of $\text{DW}_{A,s}$ for $\theta = 45^\circ$. The velocity data at temperatures above 340 K and $\epsilon_{IP} \geq 0.06$ V/nm demonstrate depinning characteristics and is fitted to eq 3. We find $\epsilon_{IP}^{C0} = 0.056$ V/nm and $\Theta = 0.736$ (bold gray line). Velocity data within the lower temperature range (300–340 K) and lower field range (0.06–0.12 V/nm) show creep behavior. The linear relationship (dashed lines) between $\ln(\bar{v})$ and $1/\epsilon_{IP}^2$, as shown in the inset, confirms a creep exponent of $\mu = 2$. The linear fits also converge at the same intercept that corresponds to $v_0 = 247$ m/s.

Domain Wall Motion Driven by In-Plane Electric Fields. The movement of $\text{DW}_{A,s}$ driven by ϵ_{OP} involves in-plane displacements of In and Se atoms near the boundary (Figure 4c–f), hinting at a potential coupling between $\text{DW}_{A,s}$ and in-plane fields. Considering the symmetry, the presence of $\text{DW}_{A,s}$ locally disrupts the C_{3v} point group symmetry, in turn generating local dipoles in $\text{DW}_{A,s}$ that could be coupled to ϵ_{IP} . This is confirmed by our finite-field MD simulations, which demonstrate ϵ_{IP} -driven $\text{DW}_{A,s}$ motion. This phenomenon is analogous to the ferroelectric domain walls investigated by Lu Guangming et al., where the bulk is nonpolar but the domain walls exhibit polarization.⁵¹ It was found that the polarization hysteresis results from the nucleation of interfaces near surfaces, followed by the evolution of the domain pattern. Moreover, monolayer α - In_2Se_3 with movable domain walls resembles the Bloch-line ferroelectrics featuring polar domain walls in paraelectric materials, as proposed by Salje and Scott.⁵² Owing to the large in-plane Born effective charges of Se and In atoms, applying ϵ_{IP} of 0.12 V/nm is sufficient to drive the movement of $\text{DW}_{A,s}$ within 100 ps at 300 K. This field strength is notably lower than what would be needed when ϵ_{OP} is applied, and is comparable to the field strengths (≈ 0.2 V/nm) used in experiments.²⁴

The ϵ_{IP} -driven $\text{DW}_{A,s}$ motion is found to exhibit a pronounced field-orientation dependence. When ϵ_{IP} is applied parallel to $\text{DW}_{A,s}$ ($\epsilon_{IP} \parallel \text{DW}$), this 1D interface shows an equal likelihood of moving either to the left or the right, corresponding microscopically to the equally probable hopping processes of Se atoms situated in proximity to $\text{DW}_{A,s}$ (Figure 6a). This behavior is a manifestation of spontaneous symmetry

breaking: while ϵ_{IP} does not inherently favor any particular direction due to the lack of physical in-plane polarization, the wall opts for a specific direction, which is induced by thermal activation. The temporal progression of the domain wall position (Figure 6a) clearly demonstrates that $\text{DW}_{A,s}$ retains the avalanche dynamics and oscillates back and forth in a stochastic manner in the case of $\epsilon_{IP} \parallel \text{DW}$. In comparison, when ϵ_{IP} is applied perpendicular to $\text{DW}_{A,s}$ ($\epsilon_{IP} \perp \text{DW}$), the wall moves deterministically, in the direction counter to that of the Se atom hopping (Figure 6b). We map out \bar{v} as a function of the relative orientation (θ) between ϵ_{IP} (of 0.1 V/nm) and the wall at 360 K, showing a strong anisotropy with the maximum velocity peaking at $\theta \approx 45^\circ$ (Figure 6c). Such highly tunable domain wall mobility in 2D ferroelectrics is beneficial for the controlled design of polarization switching speed and domain wall memory.⁵² This also highlights domain wall dynamics at reduced dimensions, as demonstrated in a recent experimental study that shows as sample thickness decreases, domain walls exhibit increased curvature and density due to dominant dipole–dipole interactions.⁵³

The T - and ϵ_{IP} -dependent mean velocity of $\text{DW}_{A,s}$ for $\theta = 45^\circ$ is displayed in Figure 6d, indicating an intrinsic creep–depinning transition.⁴³ In particular, the velocity data at temperatures exceeding 340 K overlap when $\epsilon_{IP} > 0.06$ V/nm, a hallmark feature of depinning wherein the velocity becomes temperature independent. These velocity data can be fitted to

$$\bar{v} \propto (\epsilon_{IP} - \epsilon_{IP}^{C0})^\Theta \quad (3)$$

where Θ is a velocity exponent and $\varepsilon_{\text{IP}}^{\text{CO}}$ is the crossing field at zero Kelvin. The fitting yields $\Theta = 0.736$, a value nearly identical to the reported velocity exponent of 0.72 for 90° domain walls in PbTiO_3 . This implies the existence of universal depinning dynamics for domain walls in 2D and 3D ferroelectrics. At temperatures of 340 K or lower, the velocity has a strong dependence on temperature and exhibits a nonlinear relationship with ε_{IP} , suggesting a creep behavior. As presented in the inset of Figure 6d, the velocity data in the creep region can be well described by eq 2 using the same parameters, $v_0 = 247$ m/s and $\mu = 2$, as derived from ε_{OP} -driven $\text{DW}_{\text{A},\text{s}}$ motions shown in Figure 5c. The velocity data collected under both ε_{IP} and ε_{OP} affirm the robustness of an atypical creep exponent of 2, supporting the presence of a unreported universality class.

CONCLUSIONS

Our investigation, which integrates both experimental characterizations and theoretical simulations on the ferroelectric switching in 2D $\alpha\text{-In}_2\text{Se}_3$, addresses the three aforementioned questions. First, PFM studies following rigorous protocols yield conclusive evidence indicating the absence of measurable P_{IP} in $\alpha\text{-In}_2\text{Se}_3$. Specifically, the comparative study of angle-resolved IP-PFM on both $\alpha\text{-In}_2\text{Se}_3$ and NbOI_2 demonstrates that the measured lateral response in $\alpha\text{-In}_2\text{Se}_3$ does not originate from intrinsic in-plane piezoresponse, but is due to a crosstalk artifact from the out-of-plane signal.

Second, the forbidden splitting of Wyckoff orbits for the transition from paraelectric $\beta\text{-In}_2\text{Se}_3$ to ferroelectric $\alpha\text{-In}_2\text{Se}_3$ introduces a trade-off between the robustness of P_{OP} and the difficulty in switching it: the lack of a symmetry-adapted polar mode renders P_{OP} stable against the depolarization field but also makes $\varepsilon_{\text{OP}}\text{-}P_{\text{OP}}$ coupling rather inefficient. This splitting restriction principle, along with the resultant difficulty of ε_{OP} -driven polarization reversal, is expected to be a prevalent characteristic across a wide spectrum of vdW bilayers exhibiting sliding ferroelectricity and morié ferroelectricity. The existence of domain walls, particularly $\text{DW}_{\text{A},\text{s}}$, is found to be essential for the ferroelectric switching driven by ε_{OP} in 2D $\alpha\text{-In}_2\text{Se}_3$. The giant magnitude of ε_{OP} (at the order of 1 V/nm) required for moving domain walls, as predicted by our MD simulations and corroborated by experiments,⁴ can be attributed to the weak $\varepsilon_{\text{OP}}\text{-}P_{\text{OP}}$ coupling.

Despite the lack of switchable P_{IP} in a single-domain monolayer, the presence of $\text{DW}_{\text{A},\text{s}}$ breaks the out-of-plane 3-fold rotational symmetry on a local level, allowing for a coupling between local dipoles of $\text{DW}_{\text{A},\text{s}}$ and ε_{IP} . Benefiting from the large in-plane Born effective charges and the mechanism of $\text{DW}_{\text{A},\text{s}}$ motion involving in-plane atomic displacements, applying ε_{IP} proves to be more efficient than using ε_{OP} for inducing ferroelectric switching, resolving a longstanding inconsistency between experimental observations and theoretical predictions.

We can also narrate our findings in the context of the modern theory of polarization.⁵⁴ The polarization calculated by the Berry phase method is termed *formal polarization*, which is a lattice-valued property and needs only be invariant modulo a polarization quanta under point-group operations. This means the formal polarization can be nonzero in structures with 4-fold or 3-fold rotational symmetry, such as perovskite LaAlO_3 ⁵⁵ and monolayer MoS_2 .⁵⁶ The formal polarization can

have physical consequences. For example, the discontinuity of the formal polarization at the edges of MoS_2 nanoribbons leads to metallic states.⁵⁶ Therefore, $\alpha\text{-In}_2\text{Se}_3$, similar to MoS_2 with 3-fold rotational symmetry, should exhibit in-plane formal polarization.

However, it is well established that the experimental value of the spontaneous polarization obtained from the polarization-electric field hysteresis loops should correspond to the effective polarization, which is the change in the formal polarization along the switching pathway. Our MD simulations revealed that applying an in-plane electric field to a single-domain monolayer $\alpha\text{-In}_2\text{Se}_3$ actually drives an irreversible $\alpha \rightarrow \beta'$ phase transition rather than the ferroelectric switching. For this reason, we state that single-domain monolayer $\alpha\text{-In}_2\text{Se}_3$ does not have reversible in-plane effective polarization.

Interestingly, the presence of a domain wall breaks the 3-fold rotational symmetry locally, and the discontinuity of the formal polarization causes the wall to acquire localized polarization charge. This is consistent with reports of localized polarization charges at edges or boundaries in monolayer MoS_2 nanoribbons.⁵⁶ Therefore, the motion of domain walls driven by an in-plane electric field can be heuristically understood as the electrostatically driven motion of a charged interface. This process could produce switching current in a hysteresis loop measurement as well. In this sense, it is appropriate to conclude that monolayer $\alpha\text{-In}_2\text{Se}_3$ with domain walls could exhibit in-plane effective polarization.

Finally, the 1D ferroelectric domain wall exhibits avalanche dynamics when subjected to electric fields, stemming from a competition between two distinct domain wall motion mechanisms: the conventional Miller-Weinreich line-by-line mechanism and the stone-skipping-like mechanism facilitated by an emergent high-energy interface. Our extensive data set of domain wall velocity at various temperatures and field strengths (including both ε_{OP} and ε_{IP}) reveals a creep exponent of $\mu = 2$, diverging from the known values for magnetic domain walls²⁹ and ferroelectric domain walls in bulk perovskite ferroelectrics.^{43,50}

Creep motion of a d -dimensional elastic interface moving in a $d + 1$ -dimensional random media is a physical behavior presented in a vast range of diverse systems such as vortices in type-II superconductors,⁵⁷ density waves,⁵⁸ burning⁵⁹ and wetting fronts,⁶⁰ and cell migration.⁶¹ The indication of an entirely unreported universality class associated with $\mu = 2$, as reported here, highlights the potential of 1D ferroelectric domain walls in 2D ferroelectrics for in-depth understanding of the fundamental physics of moving interfaces in reduced dimensions. Furthermore, the strong anisotropic response of domain walls to external fields and tunable onset field for the creep-depinning transition can be harnessed to configure the switching speed in 2D $\alpha\text{-In}_2\text{Se}_3$. Given the structural similarity between monolayer $\alpha\text{-In}_2\text{Se}_3$ and vdW bilayers with sliding ferroelectricity, we anticipate the atomic-level insights and quantitative understanding of domain wall mobility presented here will contribute to the comprehension of intrinsic ferroelectric switching in a broad range of 2D ferroelectrics, ultimately leading to enhanced functionalities of 2D ferroelectric-based devices.

METHODS

DFT Calculations. All first-principles density functional theory calculations are performed using the Vienna ab initio Simulation Package (VASP).^{62,63} The interaction between core ions and

electrons is modeled using the projector augmented wave (PAW) method.⁶⁴ We choose the PBE functional as the exchange–correlation functional,⁶⁵ and the van der Waals (vdW) interaction is considered using the Grimme method with a zero-damping function.⁶⁶ A slab model incorporating a vacuum layer with a thickness exceeding 20 Å along the *z*-axis is used to model monolayer In₂Se₃; the dipole correction is employed to counteract spurious interactions between periodic images across the vacuum layer. DFT calculations are based on an energy cutoff of 700 eV, a 7 × 7 × 1 Monkhorst–Pack *k*-point mesh for Brillouin zone sampling of the unit cell, and an energy convergence threshold of 10^{−8} eV for electronic self-consistency. The convergence criterion for structure optimization is set to 10^{−7} eV in energy. An external electric field is modeled by introducing a planar dipole layer at the center of the vacuum region.⁶⁷ The climbing image nudged elastic band (CL-NEB) method⁶⁸ with force convergence set to 0.01 eV/Å is used to determine the minimum energy path for polarization reversal.

Force Field of 2D α -In₂Se₃. The force field utilized in our large-scale molecular dynamics simulations is a deep neural network-based model potential, known as deep potential (DP).^{69,70} The DP model maps an atom's local environment to its energy (E_i), where the total energy E is obtained as $E = \sum_i E_i$. We have successfully trained a DP model of monolayer In₂Se₃ using a concurrent learning process that effectively updates the first-principles-based training database.⁴² The neural network architecture consists of three hidden layers, with each layer containing 240 neurons. The final training database comprises 22,600 monolayer configurations and 2163 bulk structures. With 10⁶ learnable parameters, the model has demonstrated accuracy in fitting to DFT energies and atomic forces (Figure S9). For the atomic forces of all atoms in the entire training database, the mean absolute error (MAE) and root mean squared error (RMSE) are 0.068 and 0.096 eV/Å, respectively. The model potential is capable of predicting a variety of thermodynamic properties of In₂Se₃ polymorphs (including α , β , and β'), the DFT potential energy surface for the in-plane sliding of the central Se sublayer, temperature-driven phase transitions, and energy profiles for polarization reversal and 180° domain wall motions in monolayer α -In₂Se₃ (Figure S10). We note that all local atomic environments involved in domain wall motions are well-represented in the training database (Figure S11).

Molecular Dynamics. We perform constant-temperature constant-volume (NVT) deep potential molecular dynamics simulations using LAMMPS.⁷¹ The temperature is maintained using the Nosé–Hoover thermostat and the time step is set to 1 fs. The free-standing monolayer α -In₂Se₃ containing type-A domain walls is modeled using a 20 × 40 × 1 supercell comprised of 4000 atoms and a vacuum layer of 22 Å under periodic boundary conditions, as shown in Figure S17. The effects of electric fields are modeled in classical MD simulations through the force method.⁷² This approach involves adding an additional force to each ion, calculated as the product of the ion's Born effective charge and the magnitude of the electric field. We note that at finite temperatures, the unstained free-standing monolayer α -In₂Se₃ can spontaneously transition into β' -In₂Se₃ due to their close thermodynamic stability, especially in the presence of domain walls and/or external in-plane electric fields. This is actually consistent with several experimental observations that the phase transition from α -In₂Se₃ to β' -In₂Se₃ can be induced by strain.^{10,12} To explore the intrinsic switching dynamics of 1D domain walls in monolayer α -In₂Se₃, we imposed a minor tensile strain ($\approx 1.6\%$) to stabilize the α phase and the domain walls. At a specific temperature, an equilibrium run lasting at least 1 ns is executed before the electric field is introduced to initiate domain wall movement and to measure the velocity (v) of the domain wall. The value of v is determined directly by tracking the distance traveled by the wall within a specific time frame, while also taking into account the periods of inactivity when the wall is stationary to capture the effect of avalanche dynamics. We carry out 20 independent runs (ranging from 0.1 to 1 ns) for specific temperature and electric field strength to obtain the velocity distribution of the domain wall. The methodology for determining the domain wall position during its motion relies on the coordination numbers of Se atoms. At a specific time point t (in picosecond), we

first determine the averaged structure by averaging configurations sampled every 0.1 ps within a time interval from $t - \delta$ to t , where $\delta = 1-5$ ps depending on the domain wall speed. This treatment reduces the thermal noise. We then search for the Se–In coordination within a radius of 4.2 Å centered around the Se atom. If the coordination number of a Se atom exceeds 4, we record its position, and these Se atoms define the position of the domain wall. In an effort to improve reproducibility, we have made our training database, force field model, training metadata, essential input and output files publicly available in an open repository.⁷³

Piezoresponse Force Microscopy. The PFM studies are conducted using a commercial atomic force microscope (Oxford Instrument, MFP-3D origin+). DART method is employed for PFM imaging and local switching spectroscopy measurements. Two types of conductive AFM probes with spring constants of ≈ 2.8 N/m (Asylum Research, ASYELEC.01-R2) and ≈ 0.2 N/m (Nanoworld, CONTPT) are used for cross validation and comparison. Micro-Raman spectroscopy and mapping are measured by an integrated confocal Raman microscope (Horiba, Xplora Plus) using a 532 nm laser focused by 50X long working distance objective.

ASSOCIATED CONTENT

Supporting Information

The Supporting Information is available free of charge at <https://pubs.acs.org/doi/10.1021/acsnano.4c06619>.

Comparison between dipole locking mechanism and splitting restriction principle; phase transitions during a heating–cooling cycle; previous PFM studies; Raman and SHG measurements; estimation of out-of-plane switching fields; accuracy of the DP model used in MD; sliding ferroelectricity; critical nucleus; energetics of domain walls; lifetimes of avalanche processes; dynamic walls during the stationary period; and dynamic walls during the stationary period (PDF)

AUTHOR INFORMATION

Corresponding Authors

Lu You – School of Physical Science and Technology, Jiangsu Key Laboratory of Frontier Material Physics and Devices, Soochow University, Suzhou 215006, China; orcid.org/0000-0003-3058-2884; Email: lyou@suda.edu.cn

Shi Liu – Department of Physics, School of Science and Research Center for Industries of the Future, Westlake University, Hangzhou 310030 Zhejiang Province, China; Institute of Natural Sciences, Westlake Institute for Advanced Study, Hangzhou, Zhejiang 310024, China; orcid.org/0000-0002-8488-4848; Email: liushi@westlake.edu.cn

Authors

Liyi Bai – Department of Physics, School of Science and Research Center for Industries of the Future, Westlake University, Hangzhou 310030 Zhejiang Province, China; Institute of Natural Sciences, Westlake Institute for Advanced Study, Hangzhou, Zhejiang 310024, China; orcid.org/0000-0003-3714-9151

Changming Ke – Department of Physics, School of Science and Research Center for Industries of the Future, Westlake University, Hangzhou 310030 Zhejiang Province, China; Institute of Natural Sciences, Westlake Institute for Advanced Study, Hangzhou, Zhejiang 310024, China

Zhongshen Luo – School of Physical Science and Technology, Jiangsu Key Laboratory of Frontier Material Physics and Devices, Soochow University, Suzhou 215006, China

Tianyuan Zhu – Department of Physics, School of Science and Research Center for Industries of the Future, Westlake University, Hangzhou 310030 Zhejiang Province, China; Institute of Natural Sciences, Westlake Institute for Advanced Study, Hangzhou, Zhejiang 310024, China; orcid.org/0000-0001-5007-5762

Complete contact information is available at:
<https://pubs.acs.org/10.1021/acsnano.4c06619>

Author Contributions

^{||}L.B., C.K., and Z.L. authors contributed equally.

Notes

The authors declare no competing financial interest.

ACKNOWLEDGMENTS

L.B., C.K., T.Z., and S.L. acknowledge the supports from National Natural Science Foundation of China (12304128, 52002335) and Westlake Education Foundation. The computational resource is provided by Westlake HPC Center. We thank the Research Center for Industries of the Future (RCIF) at Westlake University for partially supporting this work. We also thank Dr. Jiawei Huang for useful discussions regarding the categorization of domain walls. L.Y. acknowledges the supports from National Natural Science Foundation of China (No. 12074278) and Suzhou Science and Technology Bureau (ZXL2022514).

REFERENCES

- (1) Junquera, J.; Ghosez, P. Critical thickness for ferroelectricity in perovskite ultrathin films. *Nature* **2003**, *422*, 506–509.
- (2) Zhou, Y.; Wu, D.; Zhu, Y.; Cho, Y.; He, Q.; Yang, X.; Herrera, K.; Chu, Z.; Han, Y.; Downer, M. C.; Peng, H.; Lai, K. Out-of-Plane Piezoelectricity and Ferroelectricity in Layered α - In_2Se_3 Nanoflakes. *Nano Lett.* **2017**, *17*, 5508–5513.
- (3) Cui, C.; et al. Intercorrelated In-Plane and Out-of-Plane Ferroelectricity in Ultrathin Two-Dimensional Layered Semiconductor In_2Se_3 . *Nano Lett.* **2018**, *18*, 1253–1258.
- (4) Xiao, J.; Zhu, H.; Wang, Y.; Feng, W.; Hu, Y.; Dasgupta, A.; Han, Y.; Wang, Y.; Muller, D. A.; Martin, L. W.; Hu, P.; Zhang, X. Intrinsic Two-Dimensional Ferroelectricity with Dipole Locking. *Phys. Rev. Lett.* **2018**, *120*, No. 227601.
- (5) Wan, S.; Li, Y.; Li, W.; Mao, X.; Wang, C.; Chen, C.; Dong, J.; Nie, A.; Xiang, J.; Liu, Z.; Zhu, W.; Zeng, H. Nonvolatile Ferroelectric Memory Effect in Ultrathin α - In_2Se_3 . *Adv. Funct. Mater.* **2019**, *29*, No. 1808606.
- (6) Wan, S.; Peng, Q.; Wu, Z.; Zhou, Y. Nonvolatile Ferroelectric Memory with Lateral $\beta/\alpha/\beta$ In_2Se_3 Heterojunctions. *ACS Appl. Mater. Interfaces* **2022**, *14*, 25693–25700.
- (7) Si, M.; Saha, A. K.; Gao, S.; Qiu, G.; Qin, J.; Duan, Y.; Jian, J.; Niu, C.; Wang, H.; Wu, W.; Gupta, S. K.; Ye, P. D. A ferroelectric semiconductor field-effect transistor. *Nat. Electron* **2019**, *2*, 580–586.
- (8) Zheng, C.; et al. Room temperature in-plane ferroelectricity in van der Waals In_2Se_3 . *Sci. Adv.* **2018**, *4*, No. eaar7720.
- (9) Zhang, F.; Wang, Z.; Dong, J.; Nie, A.; Xiang, J.; Zhu, W.; Liu, Z.; Tao, C. Atomic-Scale Observation of Reversible Thermally Driven Phase Transformation in 2D In_2Se_3 . *ACS Nano* **2019**, *13*, 8004–8011.
- (10) Zheng, X.; Han, W.; Yang, K.; Wong, L. W.; Tsang, C. S.; Lai, K. H.; Zheng, F.; Yang, T.; Lau, S. P.; Ly, T. H.; Yang, M.; Zhao, J. Phase and polarization modulation in two-dimensional In_2Se_3 via in situ transmission electron microscopy. *Sci. Adv.* **2022**, *8*, No. ea-bo0773.
- (11) Chen, Z.; Sun, M.; Li, H.; Huang, B.; Loh, K. P. Oscillatory Order–Disorder Transition during Layer-by-Layer Growth of Indium Selenide. *Nano Lett.* **2023**, *23*, 1077–1084.
- (12) Han, W.; et al. Phase-controllable large-area two-dimensional In_2Se_3 and ferroelectric heterophase junction. *Nat. Nanotechnol.* **2023**, *18*, 55–63.
- (13) Stern, M. V.; Waschitz, Y.; Cao, W.; Nevo, I.; Watanabe, K.; Taniguchi, T.; Sela, E.; Urbakh, M.; Hod, O.; Shalom, M. B. Interfacial ferroelectricity by van der Waals sliding. *Science* **2021**, *372*, 1462–1466.
- (14) Rogée, L.; Wang, L.; Zhang, Y.; Cai, S.; Wang, P.; Chhowalla, M.; Ji, W.; Lau, S. P. Ferroelectricity in untwisted heterobilayers of transition metal dichalcogenides. *Science* **2022**, *376*, 973–978.
- (15) Tsymbal, E. Y. Two-dimensional ferroelectricity by design. *Science* **2021**, *372*, 1389–1390.
- (16) Wu, M.; Li, J. Sliding ferroelectricity in 2D van der Waals materials: Related physics and future opportunities. *Proc. Natl. Acad. Sci. U. S. A.* **2021**, *118*, No. e2115703118.
- (17) Wang, C.; You, L.; Cobden, D.; Wang, J. Towards two-dimensional van der Waals ferroelectrics. *Nat. Mater.* **2023**, *22*, 542–552.
- (18) Zhang, D.; Schoenherr, P.; Sharma, P.; Seidel, J. Ferroelectric order in van der Waals layered materials. *Nat. Rev. Mater.* **2023**, *8*, 25–40.
- (19) Ding, W.; Zhu, J.; Wang, Z.; Gao, Y.; Xiao, D.; Gu, Y.; Zhang, Z.; Zhu, W. Prediction of intrinsic two-dimensional ferroelectrics in In_2Se_3 and other III₂-VI₃ van der Waals materials. *Nat. Commun.* **2017**, *8*, 14956.
- (20) Xiao, C.; Wang, F.; Yang, S. A.; Lu, Y.; Feng, Y.; Zhang, S. Elemental Ferroelectricity and Antiferroelectricity in Group-V Monolayer. *Adv. Funct. Mater.* **2018**, *28*, No. 1707383.
- (21) King-Smith, R. D.; Vanderbilt, D. Theory of polarization of crystalline solids. *Phys. Rev. B* **1993**, *47*, 1651–1654.
- (22) Resta, R.; Posternak, M.; Baldereschi, A. Towards a quantum theory of polarization in ferroelectrics: The case of KNbO_3 . *Phys. Rev. Lett.* **1993**, *70*, 1010–1013.
- (23) Xue, F.; He, X.; Retamal, J. R. D.; Han, A.; Zhang, J.; Liu, Z.; Huang, J.; Hu, W.; Tung, V.; He, J.; Li, L.; Zhang, X. Gate-Tunable and Multidirection-Switchable Memristive Phenomena in a Van Der Waals Ferroelectric. *Adv. Mater.* **2019**, *31*, No. 1901300.
- (24) Wang, L.; Wang, X.; Zhang, Y.; Li, R.; Ma, T.; Leng, K.; Chen, Z.; Abdelwahab, I.; Loh, K. P. Exploring Ferroelectric Switching In_2Se_3 for Neuromorphic Computing. *Adv. Funct. Mater.* **2020**, *30*, No. 2004609.
- (25) Lente, M. H.; Eiras, J. A. 90° domain reorientation and domain wall rearrangement in lead zirconate titanate ceramics characterized by transient current and hysteresis loop measurements. *J. Appl. Phys.* **2001**, *89*, 5093–5099.
- (26) Li, L.; Wu, M. Binary Compound Bilayer and Multilayer with Vertical Polarizations: Two-Dimensional Ferroelectrics, Multiferroics, and Nanogenerators. *ACS Nano* **2017**, *11*, 6382–6388.
- (27) Yasuda, K.; Wang, X.; Watanabe, K.; Taniguchi, T.; Jarrillo-Herrero, P. Stacking-engineered ferroelectricity in bilayer boron nitride. *Science* **2021**, *372*, 1458–1462.
- (28) Cochran, W. Crystal Stability and the Theory of Ferroelectricity. *Phys. Rev. Lett.* **1959**, *3*, 412–414.
- (29) Lemerle, S.; Ferré, J.; Chappert, C.; Mathet, V.; Giamarchi, T.; Le Doussal, P. Domain Wall Creep in an Ising Ultrathin Magnetic Film. *Phys. Rev. Lett.* **1998**, *80*, 849–852.
- (30) Paruch, P.; Giamarchi, T.; Triscone, J.-M. Domain Wall Roughness in Epitaxial Ferroelectric $\text{PbZr}_{0.2}\text{Ti}_{0.8}\text{O}_3$ Thin Films. *Phys. Rev. Lett.* **2005**, *94*, No. 197601.
- (31) Paruch, P.; Guyonnet, J. Nanoscale studies of ferroelectric domain walls as pinned elastic interfaces. *C. R. Phys.* **2013**, *14*, 667–684.
- (32) Ji, J.; Yu, G.; Xu, C.; Xiang, H. General Theory for Bilayer Stacking Ferroelectricity. *Phys. Rev. Lett.* **2023**, *130*, No. 146801.
- (33) Yuan, S.; Luo, X.; Chan, H. L.; Xiao, C.; Dai, Y.; Xie, M.; Hao, J. Room-temperature ferroelectricity in MoTe_2 down to the atomic monolayer limit. *Nat. Commun.* **2019**, *10*, 1175.
- (34) Xue, F.; Zhang, J.; Hu, W.; Hsu, W.-T.; Han, A.; Leung, S.-F.; Huang, J.-K.; Wan, Y.; Liu, S.; Zhang, J.; He, J.-H.; Chang, W.-H.;

Wang, Z. L.; Zhang, X.; Li, L.-J. Multidirection Piezoelectricity in Mono- and Multilayered Hexagonal α - In_2Se_3 . *ACS Nano* **2018**, *12*, 4976–4983.

(35) Li, Y.; Chen, C.; Li, W.; Mao, X.; Liu, H.; Xiang, J.; Nie, A.; Liu, Z.; Zhu, W.; Zeng, H. Orthogonal Electric Control of the Out-Of-Plane Field-Effect in 2D Ferroelectric In_2Se_3 . *Adv. Electron. Mater.* **2020**, *6*, No. 2000061.

(36) Piner, R.; Ruoff, R. S. Cross talk between friction and height signals in atomic force microscopy. *Rev. Sci. Instrum.* **2002**, *73*, 3392–3394.

(37) Hoffmann, A.; Jungk, T.; Soergel, E. Cross-talk correction in atomic force microscopy. *Rev. Sci. Instrum.* **2007**, *78*, No. 016101.

(38) You, L.; Liu, F.; Li, H.; Hu, Y.; Zhou, S.; Chang, L.; Zhou, Y.; Fu, Q.; Yuan, G.; Dong, S.; Fan, H. J.; Gruverman, A.; Liu, Z.; Wang, J. In-Plane Ferroelectricity in Thin Flakes of Van der Waals Hybrid Perovskite. *Adv. Mater.* **2018**, *30*, No. 1803249.

(39) KüPers, M.; Konze, P. M.; Meledin, A.; Mayer, J.; Englert, U.; Wuttig, M.; Dronskowski, R. Controlled Crystal Growth of Indium Selenide, In_2Se_3 , and the Crystal Structures of α - In_2Se_3 . *Inorg. Chem.* **2018**, *57*, 11775–11781.

(40) Liu, L.; Dong, J.; Huang, J.; Nie, A.; Zhai, K.; Xiang, J.; Wang, B.; Wen, F.; Mu, C.; Zhao, Z.; Gong, Y.; Tian, Y.; Liu, Z. Atomically Resolving Polymorphs and Crystal Structures of In_2Se_3 . *Chem. Mater.* **2019**, *31*, 10143–10149.

(41) You, L.; Chen, Z.; Zou, X.; Ding, H.; Chen, W.; Chen, L.; Yuan, G.; Wang, J. Characterization and Manipulation of Mixed Phase Nanodomains in Highly Strained BiFeO_3 Thin Films. *ACS Nano* **2012**, *6*, 5388–5394.

(42) Wu, J.; Bai, L.; Huang, J.; Ma, L.; Liu, J.; Liu, S. Accurate force field of two-dimensional ferroelectrics from deep learning. *Phys. Rev. B* **2021**, *104*, No. 174017.

(43) Liu, S.; Grinberg, I.; Rappe, A. M. Intrinsic ferroelectric switching from first principles. *Nature* **2016**, *534*, 360–363.

(44) Tagantsev, A. K.; Cross, L. E.; Fousek, J. *Domains in Ferroic Crystals and Thin Films*; Springer: New York, 2010.

(45) Casals, B.; Nataf, G. F.; Salje, E. K. H. Avalanche criticality during ferroelectric/ferroelastic switching. *Nat. Commun.* **2021**, *12*, 345.

(46) Miller, R. C.; Weinreich, G. Mechanism for the Sidewise Motion of 180° Domain Walls in Barium Titanate. *Phys. Rev.* **1960**, *117*, 1460–1466.

(47) Hayashi, M. Kinetics of Domain Wall Motion in Ferroelectric Switching. I. *General Formulation*. *J. Phys. Soc. Japan* **1972**, *33*, 616–628.

(48) Tybell, T.; Paruch, P.; Giamarchi, T.; Triscone, J. Domain Wall Creep in Epitaxial Ferroelectric $\text{Pb}(\text{Zr}_{0.2}\text{Ti}_{0.8})\text{O}_3$ Thin Films. *Phys. Rev. Lett.* **2002**, *89*, No. 097601.

(49) Jo, J.; Yang, S.; Kim, T.; Lee, H.; Yoon, J.; Park, S.; Jo, Y.; Jung, M.; Noh, T. W. Nonlinear Dynamics of Domain-Wall Propagation in Epitaxial Ferroelectric Thin Film. *Phys. Rev. Lett.* **2009**, *102*, No. 045701.

(50) Shin, Y. H.; Grinberg, I.; Chen, I. W.; Rappe, A. M. Nucleation and growth mechanism of ferroelectric domain-wall motion. *Nature* **2007**, *449*, 881–884.

(51) Lu, G.; Li, S.; Ding, X.; Sun, J.; Salje, E. K. H. Ferroelectric switching in ferroelastic materials with rough surfaces. *Sci. Rep.* **2019**, *9*, 15834.

(52) Salje, E. K. H.; Scott, J. F. Ferroelectric Bloch-line switching: A paradigm for memory devices? *Appl. Phys. Lett.* **2014**, *105*, No. 252904.

(53) Scott, J. J. R.; Lu, G.; Rodriguez, B. J.; MacLaren, I.; Salje, E. K.; Arredondo, M. Evidence of the Monopolar-Dipolar Crossover Regime: A Multiscale Study of Ferroelastic Domains by In Situ Microscopy Techniques. *Small* **2024**, *20*, No. 2400646.

(54) Vanderbilt, D.; King-Smith, R. D. Electric polarization as a bulk quantity and its relation to surface charge. *Phys. Rev. B* **1993**, *48*, 4442–4455.

(55) Stengel, M.; Vanderbilt, D. Berry-phase theory of polar discontinuities at oxide-oxide interfaces. *Phys. Rev. B* **2009**, *80*, No. 241103.

(56) Gibertini, M.; Marzari, N. Emergence of One-Dimensional Wires of Free Carriers in Transition-Metal-Dichalcogenide Nanostructures. *Nano Lett.* **2015**, *15*, 6229–6238.

(57) Blatter, G.; Feigel'man, M. V.; Geshkenbein, V. B.; Larkin, A. I.; Vinokur, V. M. Vortices in high-temperature superconductors. *Rev. Mod. Phys.* **1994**, *66*, 1125–1388.

(58) Fukuyama, H.; Lee, P. A. Dynamics of the charge-density wave. I. Impurity pinning in a single chain. *Phys. Rev. B* **1978**, *17*, 535–541.

(59) Myllys, M.; Maunuksela, J.; Alava, M. J.; Ala-Nissila, T.; Timonen, J. Scaling and Noise in Slow Combustion of Paper. *Phys. Rev. Lett.* **2000**, *84*, 1946–1949.

(60) Rubio, M. A.; Edwards, C. A.; Dougherty, A.; Gollub, J. P. Self-affine fractal interfaces from immiscible displacement in porous media. *Phys. Rev. Lett.* **1989**, *63*, 1685–1688.

(61) Chepizhko, O.; Giampietro, C.; Mastrapasqua, E.; Nourazar, M.; Ascagni, M.; Sugni, M.; Fascio, U.; Leggio, L.; Malinverno, C.; Scita, G.; Santucci, S.; Alava, M. J.; Zapperi, S.; Porta, C. A. M. L. Bursts of activity in collective cell migration. *Proc. Natl. Acad. Sci. U. S. A.* **2016**, *113*, 11408–11413.

(62) Kresse, G.; Furthmüller, J. Efficient iterative schemes for ab initio total-energy calculations using a plane-wave basis set. *Phys. Rev. B* **1996**, *54*, 11169–11186.

(63) Kresse, G.; Furthmüller, J. Efficiency of ab-initio total energy calculations for metals and semiconductors using a plane-wave basis set. *Comput. Mater. Sci.* **1996**, *6*, 15–50.

(64) Blochl, P. E. Projector augmented-wave method. *Phys. Rev. B* **1994**, *50*, 17953–17979.

(65) Perdew, J. P.; Ruzsinszky, A.; Csonka, G. I.; Vydrov, O. A.; Scuseria, G. E.; Constantin, L. A.; Zhou, X.; Burke, K. Restoring the Density-Gradient Expansion for Exchange in Solids and Surfaces. *Phys. Rev. Lett.* **2008**, *100*, No. 136406.

(66) Grimme, S.; Antony, J.; Ehrlich, S.; Krieg, H. A consistent and accurate ab initio parametrization of density functional dispersion correction (DFT-D) for the 94 elements H-Pu. *J. Chem. Phys.* **2010**, *132*, No. 154104.

(67) Neugebauer, J.; Scheffler, M. Adsorbate-substrate and adsorbate-adsorbate interactions of Na and K adlayers on $\text{Al}(111)$. *Phys. Rev. B* **1992**, *46*, 16067–16080.

(68) Henkelman, G.; Uberuaga, B. P.; Jónsson, H. A Climbing Image Nudged Elastic Band Method for Finding Saddle Points and Minimum Energy Paths. *J. Chem. Phys.* **2000**, *113*, 9901–9904.

(69) Zhang, L.; Han, J.; Wang, H.; Car, R.; E, W. Deep Potential Molecular Dynamics: A Scalable Model with the Accuracy of Quantum Mechanics. *Phys. Rev. Lett.* **2018**, *120*, No. 143001.

(70) Zhang, L.; Han, J.; Wang, H.; Saidi, W. A.; Car, R.; Weinan, E. End-to-End Symmetry Preserving Inter-Atomic Potential Energy Model for Finite and Extended Systems. In *Proceedings of the 32nd International Conference on Neural Information Processing Systems*; Red Hook: NY, USA, 2018; pp. 4441–4451.

(71) Plimpton, S. Fast Parallel Algorithms for Short-Range Molecular Dynamics. *J. Comput. Phys.* **1995**, *117*, 1–19.

(72) Umari, P.; Pasquarello, A. Ab initio Molecular Dynamics in a Finite Homogeneous Electric Field. *Phys. Rev. Lett.* **2002**, *89*, No. 157602.

(73) Bai, L.; Ke, C.; Liu, S. *Intrinsic ferroelectric switching in two-dimension α - In_2Se_3* . <https://nb.bohrium.dp.tech/detail/35951125971> (accessed on Aug. 26, 2024).